Measurements and modeling of ion and neutral distribution functions in a partially ionized magnetically confined argon plasma

C. A. Michael, J. Howard, and B. D. Blackwell

Citation: Physics of Plasmas **11**, 4008 (2004); doi: 10.1063/1.1768175
View online: http://dx.doi.org/10.1063/1.1768175
View Table of Contents: http://scitation.aip.org/content/aip/journal/pop/11/8?ver=pdfcov
Published by the AIP Publishing

Measurements and modeling of ion and neutral distribution functions in a partially ionized magnetically confined argon plasma

C. A. Michael,[a] J. Howard, and B. D. Blackwell
PRL, RSPhysSE, Australian National University, Canberra ACT 0200, Australia

(Received 13 February 2004; accepted 7 May 2004; published online 16 July 2004)

The influence of ion-neutral collisions on the ion and neutral distribution functions is studied in low field (<0.15 T) rf heated argon discharges of the H-1 Heliac [S. M. Hamberger, B. D. Blackwell, L. E. Sharp, and D. B. Shenton, Fusion Technol. **17**, 123 (1990)], both experimentally and theoretically. The distribution function measurements are based on the Doppler broadening of plasma ion and neutral spectral lines using a novel coherence imaging camera. Measurements show that neutrals are abundant throughout the plasma. The neutral temperature is found to be in the range 1–2 eV, which, when compared with ion temperatures of the order of 10 eV, suggests that neutrals are being heated substantially through ion-neutral collisions. Measurements of the ion distribution function reveal a substantially elevated fraction of low energy particles (whose energy is similar to the neutral temperature), associated with charge exchange and ionization. In order to understand the origin of the high neutral temperature and distorted ion distribution function, the ion and neutral distribution functions are modeled using the Boltzmann equation including collision operators for ion-ion and ion-neutral collisions, ionization, heating, and particle loss. The simulation results compare well with the experimental results. © *2004 American Institute of Physics.*
[DOI: 10.1063/1.1768175]

I. INTRODUCTION

Neutral particle interactions with plasma ions are known to have a significant effect on plasma properties.[1,2] In this paper, we investigate the mutual influence of ion-neutral friction on both the ion and neutral distribution functions in low field ($B<0.15$ T) argon discharges of the H-1 Heliac,[3] where the plasma is produced and the electrons are heated by helicon waves.[4,5] In these discharges, the central electron density is comparable with the background neutral fill density. Radiation losses limit the attainable central electron temperature to $\lesssim 15$ eV,[6] so that the mean free path of the neutrals for ionization is comparable with the plasma radius and the plasma is only partially ionized. Because of this, the ion-ion collision rate is generally less than or equal to the charge exchange and the ionization rates. Consequently, the low energy part of the ion distribution function is significantly elevated since both charge exchange and ionization tend to produce low energy ions at a greater rate than ion-ion collisions can relax the distribution function to a Maxwellian. Conversely, the power deposited into the neutrals through ion-neutral collisions can result in substantial neutral heating.

The work presented here was also in part motivated by the observation using probes of ion temperatures substantially greater than electron temperatures.[6] Measurements of the ion distribution function might give insight into the ion heating mechanism. Spectroscopic measurements presented here show hollow ion temperature profiles, implying that the ion heating is edge localized. However, the probe measurements of the ion temperature are up to two to three times larger than spectroscopic measurements presented here. This apparent discrepancy might be at least partially due to non-Maxwellian features of the ion distribution function.

We have made spectroscopic measurements of the ion distribution function and neutral temperature, based on the Doppler broadening of ion and neutral spectral lines. At these low temperatures ($T_i \sim 10$ eV, $T_n \sim 1$ eV), a high spectral resolution ($\nu/\Delta\nu \sim 10\,000$) is required in order to resolve the spectral line, and so infer the velocity distribution function. Such measurements were made using a novel coherence imaging camera,[7–9] described in Sec. II. Since interferometric techniques are used, the instrument light throughput is up to several orders of magnitude higher than for an equivalent grating spectrometer, at high spectral resolution. In the TJ-II Heliac, measurements of the ion distribution function have been performed using a charge-exchange neutral particle analyzer.[10]

Our experimental results show the ion distribution function to be significantly non-Maxwellian. The measurements, presented in Sec. III, conform approximately to a two-temperature drifting isotropic model. We find a bulk component around 30–60 eV, and a minority cold component of fraction $\sim 30\%$ at a temperature of 3–6 eV, produced by interactions with cold neutral species, through charge exchange and ionization.

Measurements of the neutral spectral line intensity and temperature are presented in Sec. IV. Neutrals were found to be abundant throughout the plasma, consistent with previous measurements.[11] The neutral temperature was found to be ~ 1 eV, which appears to be high considering that neutrals are not confined by the magnetic field.

[a]Electronic address: Clive.Michael@anu.edu.au

To understand the distorted ion distribution function and moderate neutral temperatures, we have developed kinetic models for the ion and neutral distribution functions, incorporating the effects of charge exchange and elastic ion-neutral collisions, ionization, and ion-ion collisions. These are presented in Sec. V. The results of the kinetic modeling were consistent with the measured two-temperature ion distribution functions. To account for the moderate neutral temperatures, we found it necessary to incorporate the effects of elastic ion-neutral collisions.

II. DIAGNOSTIC AND MEASUREMENT PRINCIPLE

The coherence imaging camera is a fixed-delay imaging Fourier transform spectrometer. Information about the ion and neutral distribution functions is obtained through the Doppler broadening of plasma ion and neutral spectral lines.[7–9] Being a two-beam interferometer, the instrument measures the fringe phase ϕ and contrast ζ, at a single delay τ_0 (which is determined by the thickness of an electro-optic, birefringent wave plate). These can be combined to give the complex spectral coherence $\gamma=\zeta e^{i\phi}$. The fringes are visualized by electro-optically modulating the birefringence, and hence the delay about τ_0 using an applied ac electric field. The spread of rays through the instrument results in a reduction of the fringe contrast by a factor ζ_I and introduces a phase delay offset ϕ_I, which is also taken to include the phase offset associated with the unshifted spectral line. Instrument calibration is achieved by dividing the measured coherence γ by the instrument coherence $\gamma_I=\zeta_I e^{i\phi_I}$.[7] The instrument coherence was measured for each crystal configuration and spectral line using an expanded diffuse monochromatic light source. Hereafter, it is understood that the complex coherence has been compensated for instrumental effects.

For convenience we represent the delay in terms of the number of waves N at the unshifted spectral line frequency ν_0, given by $N=\nu_0\tau_0$. The (calibrated) complex coherence as a function of delay, $\gamma(N)$, is related to the normalized spectral line shape $g(\xi)$, where $\xi=(\nu-\nu_0)/\nu_0$ is the normalized frequency difference coordinate through a Fourier transform,[9]

$$\gamma(N)=\int g(\xi)\exp(2\pi i\kappa N\xi)d\xi, \tag{1}$$

where the quantity κ, representing the ratio of the group delay to the phase delay, is defined as

$$\kappa=1+\frac{\nu_0}{\tau_0}\frac{\partial\tau}{\partial\nu}\bigg|_{\nu_0}. \tag{2}$$

For lithium niobate crystals used, $\kappa\approx 1.6$ at 488 nm.

For a homogeneous medium, assuming that Doppler broadening is the primary line-broadening mechanism, the line shape $g(\xi)$ is a projection of the 3D distribution function $f(\mathbf{v})$ (radon transform), where $\mathbf{v}$ is in units of c, along that line of sight (direction $\hat{\mathbf{l}}$),[12]

$$g(\xi)=\int f(\mathbf{v})\delta(\xi-\mathbf{v}\cdot\hat{\mathbf{l}})d\mathbf{v}. \tag{3}$$

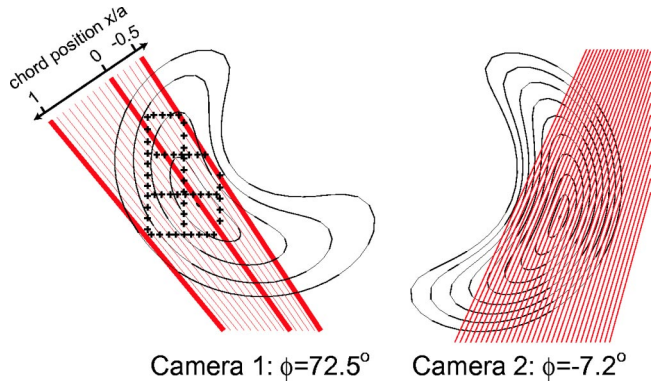

FIG. 1. Viewing chord positions for cameras installed on H-1. (Crosses denote survey points.)

When $f(\mathbf{v})$ is isotropic about a drifting frame $\mathbf{v}_d$, the line shape $g(\xi\text{-}v_d)$ is even and related to $f(v)$, the isotropic component of $f(\mathbf{v})$,

$$g(\xi-v_d)=2\pi\int_{\xi}^{\infty} f(v)v\,dv, \tag{4}$$

where $v_d=\mathbf{v}_d\cdot\hat{\mathbf{l}}$.

When the ion distribution function is Maxwellian, the projected spectral line shape $g(\xi)$ is Gaussian and so, neglecting line-integration effects (considered in the Appendix), the coherence curve is given by

$$\gamma(N)=\exp(iv_dN-\alpha N^2T), \tag{5}$$

where $\alpha=2\pi^2\kappa^2k_B/m_sc^2$ with m_s being the species mass. The temperature corresponding to each delay can be thus computed from the fringe contrast $\zeta=|\gamma|$ according to

$$T=-\frac{\ln\zeta}{\alpha N^2}. \tag{6}$$

There are two 1D coherence imaging cameras installed on H-1, viewing different poloidal cross sections as shown in Fig. 1. Camera 1, which uses a tunable grating spectrometer to select the spectral line of interest and a 16 channel detector array, has been used for neutral temperature measurements presented in Sec. IV. Camera 2 uses an interference filter to select the spectral line and has a 32 channel detector array having a more dense sampling than camera 1. This has been used for characterization of the ion distribution function.

III. MEASUREMENTS OF PROJECTIONS OF THE ION DISTRIBUTION FUNCTION

To study the ion distribution function we have made measurements of the coherence γ at several fixed optical delays. As the delay is determined by the total thickness of a combination of birefringent wave plates, multiple delay measurements were carried out on a shot-to-shot basis.

The consistency of the inferred temperature obtained for different delay plates indicates whether the ion distribution function is Maxwellian. The inferred ion temperature is plotted as a function of delay for chord positions $x/a=1$, 0, -0.5 in Fig. 2. Figure 2(a) is for a low field discharge at $B=0.06$ T, while Fig. 2(b) is for a high field discharge at

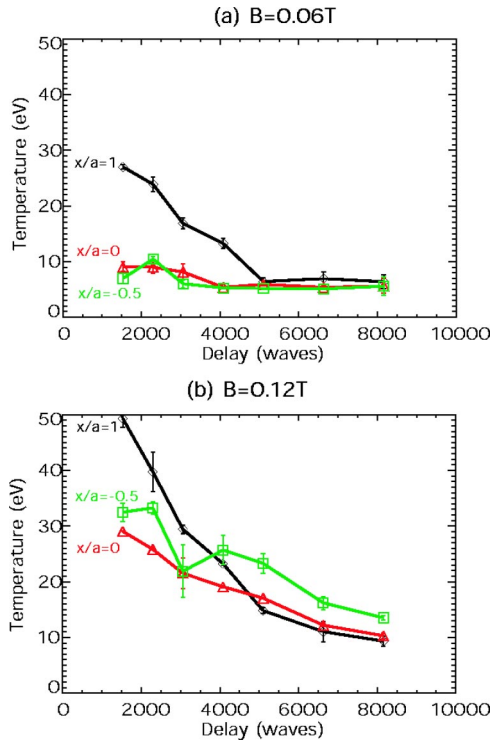

FIG. 2. Ion temperature as a function of delay for several viewing chords.

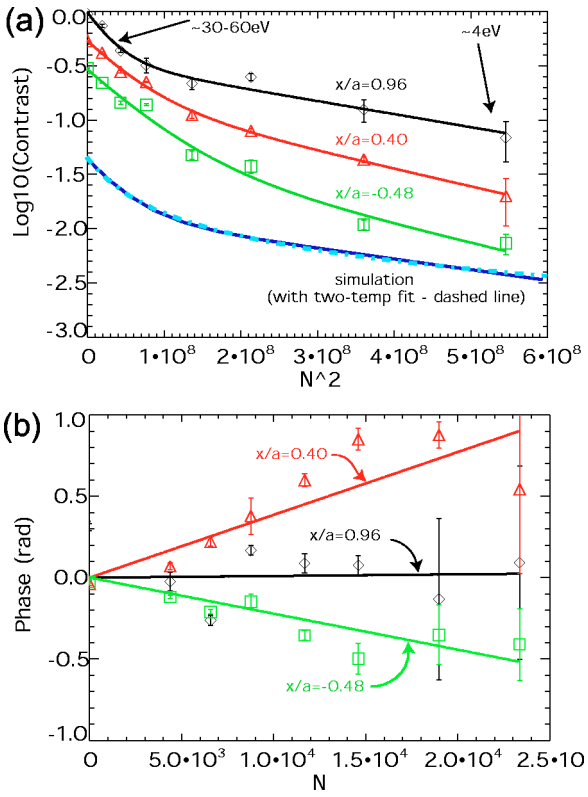

FIG. 3. (a) $\log_{10}\zeta$ vs N^2 and (b) phase vs delay, for chords at $x/a=0.96$, 0.40, and -0.48. For clarity, different chords have been displaced vertically in (a). The curves in (a) are two-temperature fits, based on Eq. (7), and the lines in (b) are lines of best fit (consistent with a drifting isotropic distribution function). The error bars were based on shot-to-shot variation. Plasma conditions are: $B=0.12$ T, $P_{\text{fill}}=36$ μTorr.

$B=0.12$ T. The low field discharge is much colder than the high field discharge, and in the interior regions conforms well with a Maxwellian since the temperature does not vary significantly with delay. In the high field discharge, the temperature varies strongly with delay for all chord positions, implying that the ion distribution function is strongly distorted. These distortions cannot be explained by integration over a spatially inhomogeneous source. This is considered in the Appendix.

To analyze in more detail the nature of the distortion to the ion distribution function we have plotted in Fig. 3 the fringe contrast and phase as functions of delay at three chord positions, for the high field discharge ($B=0.12$ T). In Fig. 3(a), we have plotted $\log_{10}\zeta$ vs N^2. It follows from Eq. (6) that a Maxwellian distribution function should produce a straight line through (1, 0) with negative slope dependent on temperature. Figure 3(b) shows a graph of ϕ vs N. For a drifting isotropic distribution function (including a Maxwellian), it follows from Eq. (4) that the spectral line shape $g(\xi-v_d)$ has even parity. Therefore, according to Eq. (1) the phase should be proportional to N.

It is clear from Fig. 3(a) that for a given viewing chord, the contrast variation with delay appears to be asymptotic to two straight lines of different slope. The steep slope at low delay corresponds to a high temperature component, while the shallower slope at high delay indicates a low temperature component. The phase variation with delay conforms approximately to a straight line, implying that the distribution function is mostly isotropic about a drifting (rotating) frame. The sign of the slope of phase shift vs delay indicates the drift direction.

The results suggest a two-temperature distribution function, which we physically interpret as a majority warm bulk component, and a cold component which is produced by interactions with neutrals, including charge exchange and ionization. We therefore fit the data points to a drifting isotropic two-temperature distribution function having contrast

$$\zeta(N)=w_b e^{-\alpha T_b N^2}+w_c e^{-\alpha T_c N^2} \tag{7}$$

with majority bulk component denoted by subscript b and minority cold component denoted by subscript c. By taking the inverse Fourier transform of Eq. (7) (to determine the line shape) and converting to a distribution function using Eq. (7), the weights w_b and w_c can be shown to represent the relative densities of bulk and cold components ($w_b+w_c=1$). The fitted curves for $\zeta(N)$ in Fig. 3(a) adequately fit the experimental measurements.

There remain components to $\phi(N)$ and $\zeta(N)$ that are not well fitted by the model. Direct Fourier transform of the complex coherence data suggests that the distribution function contains energetic, anisotropic tails which are more pronounced towards the edge of the plasma [see Fig. 2(a), $x/a=1.0$]. These tails may be driven by interactions with the sheath attached to the rf antenna and may be a source of direct ion heating. These issues are not further addressed in this paper.

The inferred parameters of the two-temperature fits of Fig. 3 are given for several chord positions in Table I. The

TABLE I. Fitted parameters of the two-temperature model for different chord positions. The error values were determined based on changes to the χ^2 residual, where there is predominantly only one degree of freedom (since one of the singular values of the covariance matrix far exceeds all others). The sign of the error values (given in parentheses) indicates the relative direction of the error (i.e., if w_c decreases then T_c and T_b must increase).

Chord position x/a	Bulk temperature T_b (eV)	Cold temperature T_c (eV)	Cold fraction w_c (%)
0.96	$61\pm(-13)$	$5.2\pm(-1.5)$	$29\pm(+6)$
0.40	$37\pm(-6)$	$7.1\pm(-1.7)$	$28\pm(+8)$
−0.48	$30\pm(-12)$	$7.3\pm(-7.8)$	$17\pm(+29)$
Simulation	39	4	28

cold component temperature is much smaller than the bulk component temperature, with the cold component fraction being around ~30%.

The cold component fraction is observed to increase with fill pressure, from ~30% at $P_{\text{fill}}=36$ μTorr to 45% at $P_{\text{fill}}=72$ μTorr. This supports the hypothesis that the cold component is being produced by ion-neutral interactions.

An independent confirmation of the two-temperature distribution was obtained using a high resolution grating spectrometer which integrates light over the duration of the plasma discharge (60 ms). The measured spectral line shape is presented in Fig. 4. It is clear that the best fit Gaussian curve is a poor match to the measured line shape. However, we find excellent agreement when compared with the line shape inferred from representative parameters for the two-temperature distribution function when convolved with the instrument function.

IV. NEUTRAL DENSITY AND TEMPERATURE PROFILE MEASUREMENTS

Ion-neutral collisions can be a significant ion energy sink. Doppler-based ion distribution function measurements have indicated the presence of a significant cold fraction, driven by ion-neutral collisions. To complete the experimental picture, we have studied the neutral density and temperature profiles by measuring the intensity and Doppler broadening of the 763 nm Ar neutral line.

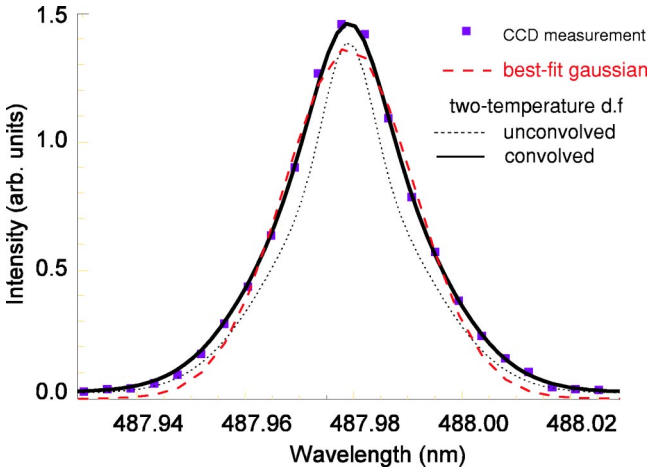

FIG. 4. Measured line shape using a grating spectrometer, together with the best-fit Gaussian, and the inferred line shape using the measurements (from the coherence imaging camera) of the two-temperature distribution function ($T_c=3$ eV, $T_b=30$ eV, cold fraction=40%).

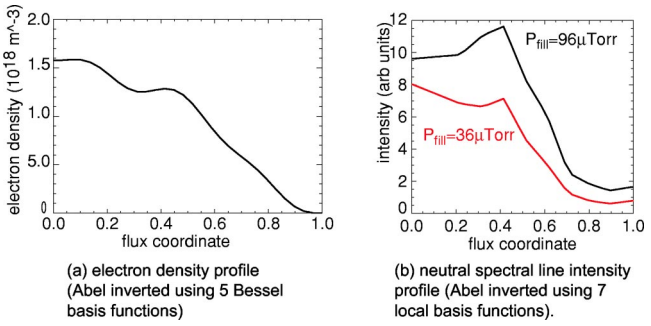

FIG. 5. Profiles (Abel inverted) of (a) the neutral intensity at two fill pressures ($B=0.12$ T) and (b) the electron density in a discharge with ($P_{\text{fill}}=36$ μTorr and $B=0.12$ T).

Assuming coronal equilibrium for the excited neutrals, the local spectral line intensity I is related to the local neutral density n_n, electron density n_e, electron temperature T_e, and excitation potential of the upper state χ_e through[13]

$$I \propto n_e n_n T_e^{-1/2} e^{-e\chi_e/kT_e}. \tag{8}$$

Given radial profiles (as functions of the flux surface coordinate) of the spectral line intensity, electron density, and temperature, we can determine the neutral density profile. A typical electron density profile obtained from a scanning far infrared (FIR) interferometer[14,15] using an Abel inversion technique is shown in Fig. 5(a). The neutral spectral line intensity profiles (after Abel inversion) at $P_{\text{fill}}=36$ μTorr and $P_{\text{fill}}=96$ μTorr are plotted in Fig. 5(b). It is clear that the neutral light intensity is flat in the center, and peaked towards the edge, and is seen to increase with fill pressure (background neutral density), while the electron density profile is generally also peaked. Given that the electron temperature does not vary significantly with radius for $r/a<0.7$,[6] we deduce that the neutral density is not significantly depleted in the center of the plasma. [A more detailed analysis of the neutral density profile using concurrent data for I, n_e, and T_e is given in Ref. 11. There it is shown that the central neutral density depletes to ~30% of the edge (fill) neutral density.] These results are consistent with estimates of the mean free path for the penetration of room temperature neutrals discussed in Sec. V B.

To reveal the nature of the neutral distribution function, we made measurements of the contrast at several fixed delays. Because the contrast degradation at the maximum available delay was small (reducing to only 80% of the maximum instrument contrast), it is difficult to ascertain whether the projection of the neutral distribution function was Maxwellian. (Kinetic modeling of the neutral distribution function in Sec. V B predicts a significantly non-Maxwellian distribution.) Nevertheless, the fixed delay inferred "temperature," which we label by T_n is useful for characterizing the width in velocity space of the neutral distribution function. The inferred neutral temperature T_n at $N=12\,000$ waves as a function of chord position x/a is plotted in Fig. 6(a) for various

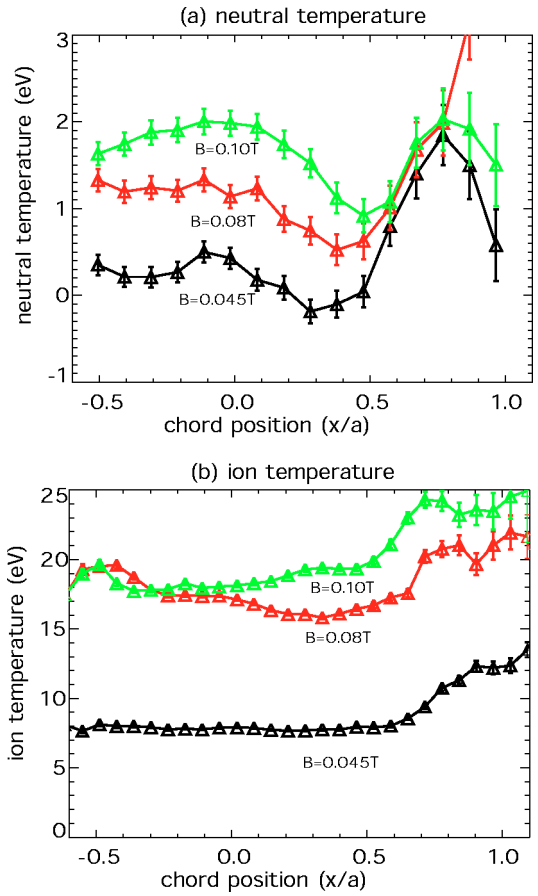

FIG. 6. Neutral and ion temperature as a function of chord position, for several magnetic field strengths ($P_{\text{fill}}=36\ \mu$Torr).

magnetic field strengths. The ion temperature, measured concurrently using camera 2 is plotted in Fig. 6(b), based on a fixed delay measurement at $N=8000$ waves.

The dependence of T_n on magnetic field strength shows a similar trend to that for the ions. This suggests that neutral heating occurs as a result of the ion-neutral interaction. Note that because the neutrals are not confined, measured neutral temperatures of 1–2 eV are not insignificant compared with the average ion temperature (of the order of 10–20 eV). The neutral temperature increases with magnetic field strength (which is associated with an increase of T_i), and the profile changes in shape. Variation of the fill pressure in the range 30–100 μTorr had little effect on the inferred neutral temperature profile. Note that Zeeman broadening of the 763 nm line is too small ($\sim$0.13 eV) to account for either the magnitude or shape of the neutral temperature profiles.

V. KINETIC MODELING OF ION-NEUTRAL INTERACTIONS

In order to account for the observed cold component of the ion distribution function and moderate neutral temperatures, we model the (isotropic) velocity space ion and neutral distribution functions under the influence of charge exchange and elastic ion-neutral collisions using the Boltzmann equation.

A. Ion distribution function

Nonthermal features in a species distribution function can arise when the particle and/or energy confinement times are shorter than the like particle collision time. The ionization rate can be used to estimate the particle confinement time, and the charge-exchange rate contributes to the energy confinement time. Both ionization and charge exchange strongly replenish the ion distribution function at low energies, thereby distorting it away from a Maxwellian.

Taking the value for the charge-exchange cross section as $\sigma_{CX}=50$ Å^2,[16] and the ionization rate given through the exchange classical impact parameter approximation,[13] it can be shown that the ion-neutral charge-exchange rate ν_{in} and ionization rate ν_{iz} normalized to the ion-ion collision rate ν_{ii} are given by

$$\nu_{in}/\nu_{ii}=\left(\frac{T_i}{8.9\ \text{eV}}\right)^2\frac{n_n}{n_i}, \tag{9}$$

$$\nu_{iz}/\nu_{ii}=0.71e^{-\chi_i/T_e}\sqrt{T_e/\chi_i}T_i^{3/2}\frac{n_n}{n_i}, \tag{10}$$

for T_i given in eV, and where the ionization potential, $\chi_i=15.1$ eV. For typical H-1 parameters, $T_e=T_i=10$ eV, and $n_i=n_n$, we find $\nu_{in}/\nu_{ii}\sim 1$ and $\nu_{iz}/\nu_{ii}=4.13$, so that both processes will appreciably drive the distribution function away from Maxwellian form.

1. Model description

We solve for the equilibrium ion distribution function $f_i(v)$ (which, for simplicity, we assume to be isotropic and homogeneous) by solving the Boltzmann equation, which for the ions can be expressed as

$$\frac{\partial f_i}{\partial t}+\mathbf{v}\cdot\nabla f_i+\frac{e}{m}(\mathbf{E}+\mathbf{v}\times\mathbf{B})\cdot\nabla_{\mathbf{v}}f_i$$
$$=C_{ii}(f_i)+C_{in}(f_i,f_n)+C_{iz}(f_n,f_e). \tag{11}$$

Here C_{ii} is the ion-ion collision operator, C_{in} represents ion-neutral collisions, and C_{iz} is the source term for ionization. In steady state, the left-hand side of the equation, $\mathbf{v}\cdot\nabla f_i+(e/m)(\mathbf{E}+\mathbf{v}\times\mathbf{B})\cdot\nabla_{\mathbf{v}}f_i$ represent the effects of confinement by the electric and magnetic fields, as well as the heating effects of the wave-particle interactions. In order to handle these terms rigourously, it would be necessary to take account of the spatial variations of f_i, f_n, and f_e and to have an accurate kinetic description of the ion heating mechanism. Until the ion heating mechanism in H-1 is better understood, it is not possible to make such a full description of these terms.

We proceed with a spatially homogeneous kinetic description based on simple forms for particle loss and heating [represented by the left-hand side of Eq. (11)]. We postulate that these terms can be effectively replaced by operators for heating, $C_h(f_i)$, and particle loss, $C_l(f_i)$,

$$\mathbf{v}\cdot\nabla f_i+\frac{e}{m}(\mathbf{E}+\mathbf{v}\times\mathbf{B})\cdot\nabla_{\mathbf{v}}f_i=-C_l(f_i)-C_h(f_i). \tag{12}$$

Equation (11) therefore can be expressed as

$$\frac{\partial f_i}{\partial t} = C_{\text{tot}}, \tag{13}$$

where, C_{tot} is defined as

$$C_{\text{tot}} = C_{ii}(f_i) + C_{in}(f_i, f_n) + C_{iz}(f_n, f_e) + C_h(f_i) + C_l(f_i). \tag{14}$$

The particle loss operator can be defined simply through a velocity dependent loss rate $\nu(v)$,

$$C_l = -f_i(v)\nu(v). \tag{15}$$

As an ansatz, we assume that ν increases in proportion to v, defining a scale length d such that

$$\nu(v) = v/d. \tag{16}$$

The heating operator, which is particle conserving, couples energy to the distribution function through wave-particle interactions, resulting in an average net acceleration of all particles. To elucidate the nature of C_h, we introduce the function $P(v,\Delta v)$ to be the probability that a particle of speed v will be accelerated to speed $v+\Delta v$ in a time Δt. By linearizing the operator P, and neglecting second-order terms, we identify the generalized heating operator $C_h(v)$,[17]

$$C_h(v) = \frac{1}{v^2}\frac{\partial}{\partial v}[\bar{a}(v) f(v) v^2], \tag{17}$$

where $\bar{a}$ is the average acceleration with respect to the probability distribution function P,

$$\bar{a}(v) = \int P(v, a\Delta t) a\, da. \tag{18}$$

In the absence of any detailed knowledge of the ion heating mechanism, we impose the ansatz that the average acceleration is independent of velocity,

$$\bar{a}(v) = \text{const}. \tag{19}$$

For modeling ion-neutral collisions, we consider only charge exchange, for which the collision operator can be expressed simply as[17]

$$C_{in}(f_i) = \xi_{in}(n_i f_n - n_n f_i), \tag{20}$$

where $\xi_{in} = \langle \sigma_{CX} v \rangle$ is the charge-exchange rate coefficient. For the ionization collision operator, we take

$$C_{iz} = n_i \xi_{iz} f_n, \tag{21}$$

where ξ_{iz} is the ionization rate coefficient and can be determined using the classical exchange approximation.[13] For the ion-ion collision operator we have used the isotropic form of the Fokker-Planck-Landau Coulomb collision operator.[18] The Krook collision operator cannot be used because of the large gradients in velocity space caused by the influx of particles at the neutral temperature due to ionization and charge exchange.

The equilibrium distribution function f is obtained by solving the Boltzmann Eq. (11) using relaxation techniques. An explicit iterative scheme is used

$$f_i^{k+1} = f_i^k + \Delta t C_{\text{tot}}^k, \tag{22}$$

where superscripts refer to the time-step index, Δt is the time-step interval, and C_{tot} is given in Eq. (14).

We impose the condition that the density and average energy remain at their initial values by defining the parameters $\bar{a}$ and d at each step in the iteration such that the zeroth and second moments of C_{tot} are zero. We assign the initial function $f_i(v)$ to be a Maxwellian with density and temperature appropriate to the measured values. With the moments of f_i fixed, the relaxation allows only for a distortion of the distribution function away from Maxwellian form.

Since the heating operator C_h is particle conserving (having its zeroth moment equal to zero), the zeroth moment of C_l (the net particle loss rate) must be balanced by the zeroth moment of C_{iz} (the net particle ionization rate),

$$\underbrace{C_l^{(0)}}_{<0} = -\underbrace{C_{iz}^{(0)}}_{>0}, \tag{23}$$

where $C^{(n)}$ is the nth velocity moment defined as $C^{(n)} = \int C(v) v^{n+2} dv$. Using Eqs. (15) and (16), the parameter d is determined by

$$d = \frac{\int f_i(v) v^3 dv}{\int C_{iz}(v) v^2 dv}. \tag{24}$$

The total power input equal to the second moment of $C_h + C_{iz}$ must be balanced by the power lost through ion-neutral collisions and particle loss,

$$\underbrace{C_h^{(2)}}_{>0} + \underbrace{C_{iz}^{(2)}}_{>0} = -\left(\underbrace{C_{in}^{(2)}}_{<0} + \underbrace{C_l^{(2)}}_{<0}\right) \tag{25}$$

and so $\bar{a}$ is determined by

$$\bar{a} = -\frac{\int (C_l(v) + C_{iz}(v) + C_{in}(v)) v^4 dv}{\int \frac{\partial}{\partial v}(f v^2) v^2 dv}. \tag{26}$$

2. Simulation results and comparison with experiment

There are three input parameters for the simulation: the initial ion temperature T_{i0}, the electron temperature T_e, and the ratio of the neutral density to the ion density (n_n/n_i). Since accurate measurements of the electron temperature and neutral density are not available, we do not attempt to make a detailed comparison with the experimental results. Nevertheless, the modeling results show that the gross features of the computed distribution function appear not to be sensitively dependent on the chosen input parameters.

For comparison with the high field ($B = 0.12$ T) discharge shown in Fig. 3, we take the initial temperature T_{i0} to be 40 eV, estimate $T_e = 8$ eV based on probe data,[6] and assume $n_n/n_i = 30\%$ according to estimates given in Ref. 11.

The initial and relaxed distribution functions are shown in Fig. 7 together with a two-temperature distribution obtained by fitting to the corresponding coherence curve $\gamma(N)$ (the Fourier transform of the projection of f) given in Fig. 3.

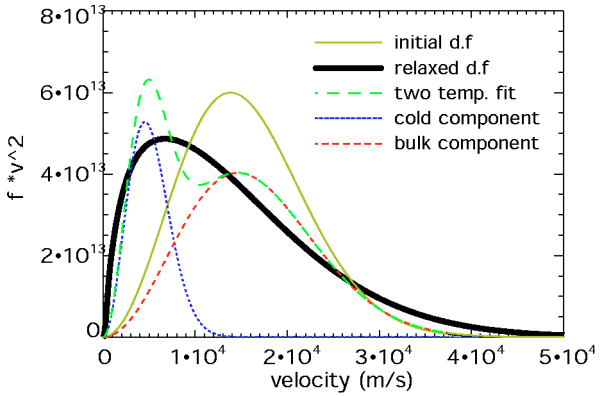

FIG. 7. Relaxed distribution function, together with a two-temperature fit (where the parameters are determined from the coherence curve in Fig. 3). The initial Maxwellian distribution (with the same rms velocity) is also shown.

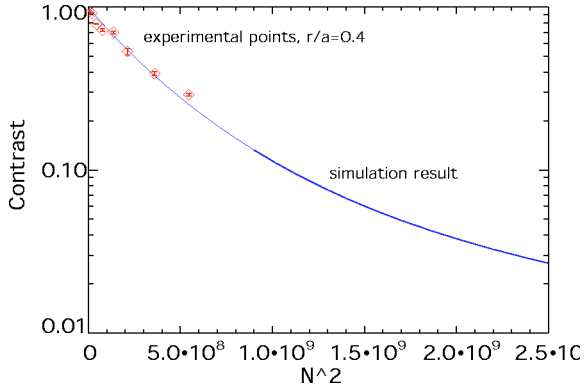

FIG. 9. Contrast, based on the computed distribution function, as a function of N^2 for the ions for the low field ($B=0.06$ T), low temperature discharge, together with the experimental measurements. (Note the extended range for N^2, compared with Fig. 3, showing the two-temperature characteristics of the modeling results.)

As is required by the constraint equation (25), the initial and final distributions have the same rms velocity. The final ion distribution differs significantly from a single temperature Maxwellian, there being an elevated population of cold particles (whose energy is of the order of the neutral temperature) and a residual energetic component required by the second moment constraint. It is also clear that the two-temperature distribution function does not adequately describe the features of the relaxed velocity distribution function. (However, the difference between the velocity-space projections of the relaxed and two-temperature distributions are indiscernible. We return to this point later.)

The constituent collision operators of the final relaxed distribution function are plotted in Fig. 8. As expected, ionization and charge exchange tend to populate the lower energy components, while ion-ion collisions and heating deplete the lower energy population to produce higher energy particles. The particle loss term is much smaller than other collision operators.

The coherence curve $\gamma(N)$, obtained from the Fourier transform of the projection of $f(v)$ along the line of sight, together with a two-temperature fit is compared with the experimental data in Fig. 3. It can be seen from the figure that the two-temperature model describes $\gamma(N)$ very well, even though it does not accurately reproduce the modeled distribution function. This is due to the low-pass filter properties of the Doppler projection (3D Radon transform), given in Eq. (4). The parameters of the two-temperature fit (of the simulated distribution function), which are given in Table I, are similar to the experimental measurements at $x/a=1.0$.

We have also modeled the distribution function for the low field ($B=0.06$ T), low temperature ($T=4$ eV) discharge given in Fig. 2(a). To match the measurements, we chose $T_{i0}=6$ eV, with $n_n/n_i=30\%$ and $T_e=8$ eV (being the same as used previously). The coherence curve for the relaxed ion distribution function is plotted together with the experimental measurements for two chord positions in Fig. 9. It is clear that within the range of measurement ($N<15\,000$), the distribution function appears Maxwellian, in agreement with the measurements of Fig. 2(a). However, at larger values of N, the two-temperature characteristics of the simulated coherence curve become apparent.

Since the electron temperature and neutral density are not accurately known, it is worthwhile to explore the sensitivity of the simulated distribution function to these parameters in order to assess the validity of the comparison [in the case of high field ($B=0.12$ T) discharge]. The cold component temperature T_c and fraction w_c obtained from fits to simulation results are plotted as a function of n_n/n_i in Fig. 10. It is clear that as the strength of the cold neutral source is increased, the cold component fraction reaches a saturation level at $\sim 40\%-50\%$, and the cold component temperature remains roughly constant at 5–6 eV. Given that the cold component is produced by collisions with neutrals, the temperature of the cold component must remain small. The saturation of the cold component fraction is a consequence of the fact that the model enforces the second moment of f to remain constant throughout the relaxation. Therefore, as n_n/n_i increases, the heating collision operator C_h must increase to balance the power lost through charge exchange and particle loss. As C_h depletes the population of cold particles, this effectively limits the cold component fraction.

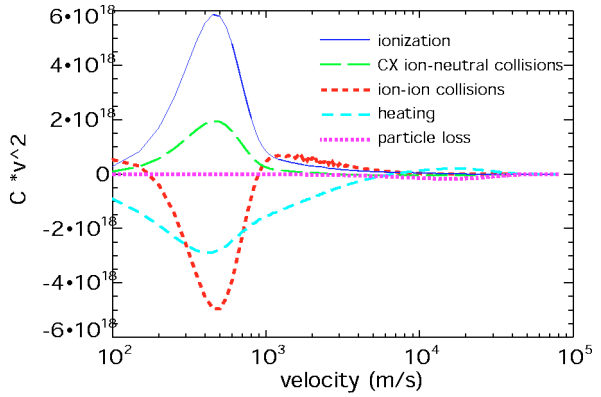

FIG. 8. Constituent collision operators for the relaxed distribution function in Fig. 7.

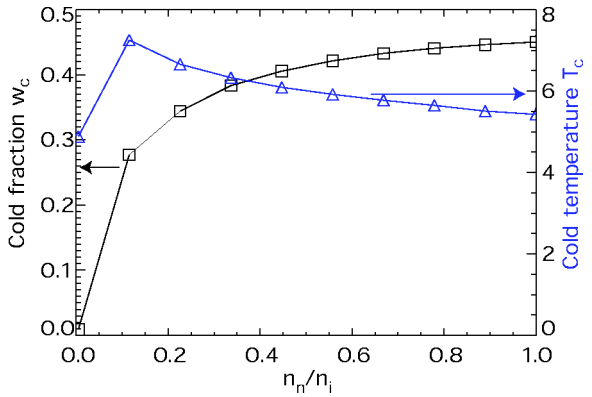

FIG. 10. Parameters of the two-temperature fit to the simulated distribution functions, T_c and w_c, as a function of n_n/n_i.

B. Neutral distribution function

The penetration and kinetics of neutrals in fusion plasmas have been a topic of much interest.[1] A simple view of the dynamics can be obtained by regarding the neutrals as comprising two independent (Maxwellian) populations: a slow component, at the temperature of the background gas, and a fast component at the ion temperature, driven by charge exchange. Both slow and fast neutrals are depleted directly by ionization. Based on a fluid model, assuming constant density and temperature, it has been shown[2] that the penetration length scale for slow (L_s) and fast (L_f) neutrals is given by

$$L_s=\frac{v_{tn}}{n_i\sqrt{(\xi_{iz}+\xi_{ins})(2\xi_{iz}+\xi_{ins})}}, \tag{27}$$

$$L_f=\frac{v_{ti}}{n_i\sqrt{\xi_{iz}(2\xi_{iz}+\xi_{inf})}}, \tag{28}$$

where $\xi_{iz}=\langle\sigma_{iz}v\rangle$ is the rate coefficient for ionization, and $\xi_{ins}=\langle\sigma_{in}v\rangle_s$, $\xi_{inf}=\langle\sigma_{in}v\rangle_f$ are the rate coefficients for ion-neutral collisions from the slow and fast populations, respectively.

The applicability of this model is limited, as it neglects the finite size of the plasma and assumes constant density and temperature. However, by comparing L_s and L_f with the plasma minor radius a, we can assess whether neutrals penetrate ballistically or diffusively. In H-1, for $n_i=n_e=0.5\times10^{18}$ m^{-3}, $T_i=20$ eV, $T_e=8$ eV, $T_n=300$ K, and given ξ_{iz} from Ref. 13, we find $L_s=4$ cm$<a$ and $L_f=100$ cm$>a$ ($a=15$ cm). Therefore, fast neutrals are ballistic (within the plasma volume) while slow neutrals are collisional.

In our analysis of the neutral distribution function, we neglect the effects of wall recycling of fast neutrals, which would tend to increase the fast neutral population. Since the H-1 Heliac features a ''coil-in-tank'' design, the greatest effect of wall recycling is expected to arise from collisions with the coils and support structure. We estimate the albedo of the neutrals for collisions with the near-facing support structure to be $\sim$50%, since the spacing of toroidal coils is of the same order as their width. Most neutrals which penetrate the support structure do not return to the plasma, since the volume of the vacuum vessel is $\approx$30 times the plasma volume.

To show the influence of charge-exchange and elastic collision processes on the neutral distribution function, we first consider a simple model for determining the equilibrium fraction of fast particles by balancing the fast neutral ''birth rate'' (due to ion-neutral collisions) with the loss rate, determined by the average speed $\overline{v_f}$ of fast particles streaming out of the plasma volume, across a distance a,

$$n_n n_i \xi_{in}=\frac{\overline{v_f}}{a}n_f. \tag{29}$$

If we assume that only charge-exchange collisions produce ''fast'' neutrals, then $\overline{v_f}=v_{ti}$ (the ion thermal velocity) and the charge-exchange neutral fraction becomes $n_f/n_n=an_i\sigma_{CX}$. For typical plasma parameters ($n_i=0.5\times10^{18}$ m^{-3}, $T_n=300$ K, $T_i=10$ eV), $n_f/n_n\sim2.5\%$, which is not sufficient to account for the measured neutral temperatures. On the other hand, if we neglect charge-exchange collisions and assume that fast neutrals (compared with the room temperature background) are produced only by elastic ion-neutral collisions, then clearly $\overline{v_f}<v_{ti}$. Since the cross section for elastic ion-neutral collisions is similar to that of charge exchange (in the range 1–10 eV),[16,19] then based on Eq. (29), the fraction of elastically scattered fast neutrals is expected to be much higher.

To more accurately quantify the kinetics of the collision processes and their influence on the neutral distribution function, we employ the Boltzmann equation to solve for the neutral distribution function, using the kinetic collision operator ion-neutral collisions (C_{in}), incorporating both elastic and ion-neutral collisions,

$$\frac{\partial f_n}{\partial t}+C_v(f_n)=C_{in}(f_n,f_i)+C_{iz}(f_n,f_e), \tag{30}$$

where we have denoted the convective derivative by $C_v(f_n)=\mathbf{v}\cdot\nabla f$. The collision operator C_{in} can be derived from the differential elastic scattering cross section. Conventionally, the charge-exchange component arises from reverse scattering (for which the scattering angle $\theta>\pi/2$), while the elastic scattered component arises from forward scattering ($\theta<\pi/2$). We obtained the differential scattering cross section for elastic and charge-exchange ion-neutral collisions in argon from Ref. 20.

In order to solve the problem rigorously, it would be necessary to take into account the full spatial dependence of f_n and allow for anisotropy. This problem may be tractable through the use of a high-order moment approach.[21] In our approach, we reduce the problem to a solvable form by assuming f_n is isotropic, neglecting ionization and idealizing the spatial dependence of f_n. The first assumption allows for simpler computation of C_{in}. We neglect ionization since it depletes the neutral distribution function uniformly over all velocities, thereby not affecting the temperature or rms velocity. This assumption would give erroneous results for the neutral density, however, we seek only to account for the

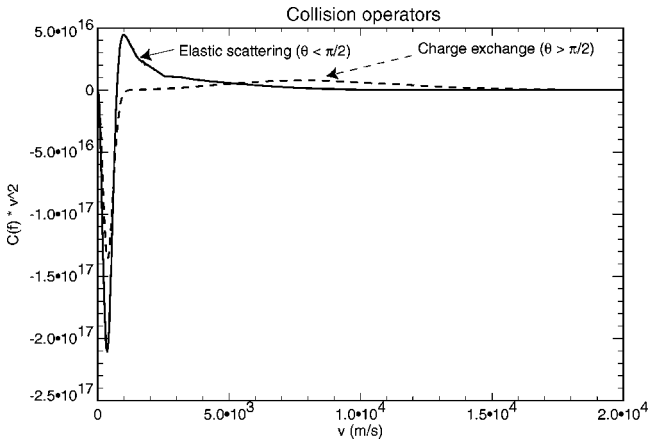

FIG. 11. Charge-exchange and elastic scattering collision operators, evaluated for Maxwellian ion and neutral distribution functions. The function has been weighted by the volume element v^2. Parameters are $T_i=10$ eV, $T_n=300$ K, $n_i=n_n=10^{18}$ m^{-3}.

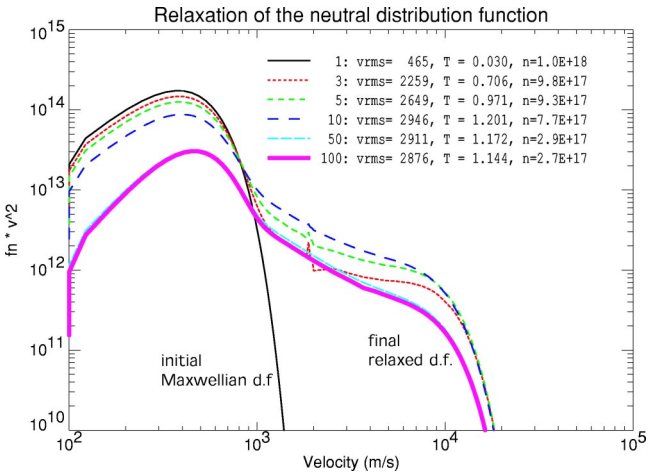

FIG. 12. Relaxation of the neutral distribution function at successive iterations. Indicated are v_{rms}, $T=\frac{1}{3}mv_{rms}^2$, and density for each iteration. Parameters used are $T_{n0}=300$ K, $T_i=10$ eV, $n_n=n_i=10^{18}$ m^{-3}, and time-step interval $\Delta t=10^{-5}$ s.

measured neutral temperature. Following the third simplification, we approximate the convective particle loss operator by

$$C_v(v)=v\frac{f_n-f_{n1}}{a}, \tag{31}$$

where f_n is the neutral distribution function at the center of the plasma and f_{n1} is the neutral distribution function at the periphery of the plasma (defined to be a Maxwellian of temperature 300 K and density n_{fill} given by the fill pressure). This accounts for the loss of (fast) neutrals from the plasma as well as the replenishment of room temperature neutrals from outside the plasma volume.

The isotropic ion-neutral collision operator was computed from the differential scattering cross section using the standard form in spherical polar coordinates.[22] For the integration over four variables for each value of v, we use the NAG routine d01fcf. For the ion distribution function, we assume a Maxwellian, though we have shown the presence of non-Maxwellian ion distribution functions. This is not expected to have a large influence on the ion-neutral collision operator.

The computed charge-exchange and elastic collision operators (assuming $f_n=f_{n1}$) are compared in Fig. 11. It can be seen that, while charge exchange populates the neutrals at the ion thermal velocity, elastic collisions populate the neutrals at a much lower intermediate velocity of $v\approx 3-5v_{tn}$.

1. Results and comparison with experiment

The neutral distribution function f_n is relaxed in time from f_{n1} (defined above) according to an explicit scheme. The evolution of the distribution function from the initial to final states is shown in Fig. 12. The distribution is seen to distort from Maxwellian, populating higher energies.

To compare the modeling results directly with experimental data of Sec. IV, we compute the coherence curve $\gamma(N)$ from the Fourier transform of the line shape, which is obtained using Eq. (4). Based on $\gamma(N)$, we then calculate the equivalent Maxwellian temperature T_n based on a the single delay used for the experiment ($N=12\,000$). We found that T_n was within a factor of 2 of the average energy. By running the simulation at different plasma parameters, we obtained an appropriate scaling law: $T_n\propto T_i^{0.66}n_i^{0.86}$, closely related to the ion pressure. Consistent with the observation that T_n is independent of n_{fill}, the velocity dependence of the Boltzmann equation (30) can also be shown to be independent of n_{fill}.

The measured and computed values of fixed delay temperature T_n at $N=12\,000$ waves are plotted as a function of the determined scaling law in Fig. 13, showing approximate agreement between the two. The larger experimental values may be accounted for by wall recycling. This corroborates the notion that the observed neutral temperatures can be explained through elastic ion-neutral collisions.

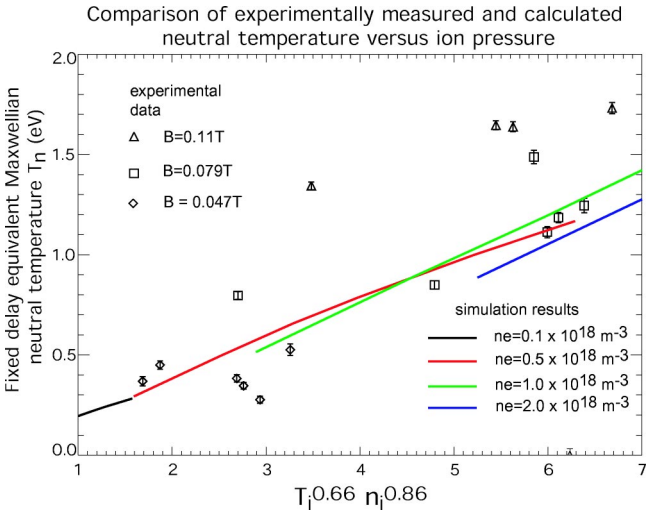

FIG. 13. Comparison of the measured and computed values of T_n as a function of the appropriate scaling law of the ion density and temperature.

VI. CONCLUSION

The high light throughput and spectral resolution of the recently developed coherence imaging camera has enabled detailed spectroscopic measurements to be made of the ion distribution function and neutral temperature in a magnetically confined, partially ionized argon plasma in the H-1 Heliac. These measurements were initially undertaken in order to obtain some insight into the ion heating mechanism and to resolve apparent inconsistencies between probe and spectroscopic measurements of the ion temperature. Results have shown that the ion distribution function is significantly non-Maxwellian, with the most striking feature being an elevated fraction of cold ions. We have investigated this theoretically and found that the cold component is produced by charge exchange with neutrals and ionization. The strong influence of the neutrals on the ions motivated us to measure the neutral temperature, which we found to be of the order of 1 eV. This is quite high considering the lack of magnetic confinement, though not inconceivable given the amount of power that the neutrals absorb from the ions.

To provide a theoretical understanding of the measurements, simple, zero-spatial dimensional, isotropic kinetic models of the ion and neutral distribution functions have been developed, based on the Boltzmann equation. Consistent with the measurements, we found the model predicted a substantial fraction of cold ions, associated with charge exchange and ionization. Concomitantly, the computed neutral distribution function was also found to be non-Maxwellian, with moderate average energies around 1 eV. Elastic ion-neutral collisions were found to be the primary mechanism responsible for neutral heating, as charge-exchange neutrals promptly depart the plasma. Satisfactory agreement was obtained between the calculations and the measurements.

Further investigations of the anisotropic energetic tail components of the ion distribution function, reported in Sec. III, could reveal new information about the ion heating mechanism, which is so far not well understood.

ACKNOWLEDGMENT

The authors gratefully acknowledge the assistance of R.W. Boswell for valuable discussions and checking the manuscript.

APPENDIX: LINE-INTEGRATION EFFECTS ON THE COHERENCE MEASUREMENT

In this appendix, we estimate the distortion to the line shape and coherence arising from line integration through an inhomogeneous source. Assuming that the ion distribution function is a locally drifting Maxwellian, distortions to the line shape (from Gaussian form) can arise from variations in the Doppler shift (flow speed v_d) as well as variations in the Doppler broadening (temperature T, with thermal velocity v_{th}) along the line of sight. We denote line-integrated quantities (weighted by intensity) with $\check{}$.

It can be shown that,[23] to first order in $\check{v}_d/\check{v}_{th}$, the line-integrated line shape $\check{g}(\xi-\check{v}_d)$ is an even function, related to the locally unshifted line shape $g(\mathbf{r},\xi-v_d(\mathbf{r}))$ and local emissivity $I_0(\mathbf{r})$ according to

$$\check{I}_0\check{g}(\xi-\check{v}_d)=\int I_0(\mathbf{r})g(\mathbf{r},\xi-v_d(\mathbf{r}))dl. \tag{A1}$$

Since $\check{v}_d/\check{v}_{th}\simeq 10\%$, the distortion due to variations in the flow along the line of sight is of order 1%. We therefore need only to consider the effect of a variation in temperature along the line of sight.

It can be shown that the line-averaged contrast $\check{\zeta}$ decreases with the parameter $x=(\pi\kappa N\check{v}_{th})^2$ according to

$$\check{\zeta}=e^{-x}\left(1+\frac{1}{2}x^2\frac{T_{rms}^2}{\check{T}^2}\right), \tag{A2}$$

where

$$T_{rms}^2=\check{I}_0^{-1}\int I(\mathbf{r})(T(\mathbf{r})-\check{T})^2dl. \tag{A3}$$

For a hollow temperature profile, with edge temperature being twice the central temperature, the computed value of $T_{rms}/\check{T}\approx 0.25$. Therefore, for example, at $x=2$ (where the contrast degradation is $e^2\sim 8\%$), the fractional error in the contrast will be $\approx 20\%$. This is insufficient to account for the elevated contrast at large delays, as shown in Fig. 3.

[1] M. Tendler and D. Heifetz, Fusion Technol. **11**, 289 (1987).
[2] B. Lehnert, Phys. Scr. **12**, 327 (1975).
[3] S. M. Hamberger, B. D. Blackwell, L. E. Sharp, and D. B. Shenton, Fusion Technol. **17**, 123 (1990).
[4] P. K. Loewenhardt, B. D. Blackwell, and S. M. Hamberger, Plasma Phys. Controlled Fusion **37**, 229 (1995).
[5] R. W. Boswell, Plasma Phys. Controlled Fusion **26**, 1147 (1984).
[6] M. G. Shats, D. L. Rudakov, R. W. Boswell, and G. G. Borg, Phys. Plasmas **4**, 3629 (1997).
[7] J. Howard, C. Michael, F. Glass, and A. D. Cheetham, Rev. Sci. Instrum. **72**, 888 (2001).
[8] C. A. Michael, J. Howard, and B. D. Blackwell, Rev. Sci. Instrum. **72**, 1034 (2001).
[9] J. Howard, C. Michael, F. Glass, and A. Danielsson, Plasma Phys. Controlled Fusion **45**, 1143 (2003).
[10] F. Castejon, R. Balbin, A. Lopez *et al.*, Rev. Sci. Instrum. **74**, 1795 (2003).
[11] H. Punzmann, M. G. Shats, W. M. Solomon, and H. Xia, Rev. Sci. Instrum. **74**, 2048 (2003).
[12] C. A. Michael, Ph.D. thesis, Australian National University, 2003.
[13] I. H. Hutchinson, *Principles of Plasma Diagnostics* (Cambridge University Press, Cambridge, 1987).
[14] J. Howard, Rev. Sci. Instrum. **61**, 1086 (1990).
[15] G. B. Warr, B. D. Blackwell, J. Wach, and J. Howard, Fusion Eng. Des. **34–35**, 387 (1997).
[16] S. H. Pullins, R. A. Dressler, R. Torrents, and D. Gerlich, Z. Phys. Chem. (Munich) **214**, 1279 (2000).
[17] R. D. Hazeltine and F. L. Waelbroeck, *The Framework of Plasma Physics* (Perseus Books, Reading, MA, 1998).
[18] W. MacDonald, M. N. Rosenbluth, and W. Chuck, Phys. Rev. **107**, 350 (1957).
[19] A. V. Phelps, J. Appl. Phys. **76**, 747 (1994).
[20] M. L. Vestal, C. R. Blakley, and J. H. Futrell, Phys. Rev. A **17**, 1337 (1978).
[21] K. Kumar, H. R. Skullerud, and R. E. Robson, Aust. J. Phys. **33**, 343 (1980).
[22] R. L. Liboff, *Kinetic Theory: Classical, Quantum, and Relativistic Descriptions* (Prentice Hall, Englewood Cliffs, NJ, 1990).
[23] J. Howard, Plasma Phys. Controlled Fusion **38**, 489 (1996).